Article

Strain-Engineered van der Waals Interfaces of Mixed-Dimensional Heterostructure Arrays

Baishan Liu, Qingliang Liao, Xiankun Zhang, Junli Du, Yang Ou, Jiankun Xiao, Zhuo Kang, Zheng Zhang, and Yue Zhang

ACS Nano, **Just Accepted Manuscript** • DOI: 10.1021/acsnano.9b03239 • Publication Date (Web): 19 Jul 2019

Strain-Engineered van der Waals Interfaces of Mixed-Dimensional Heterostructure Arrays

Baishan Liu[1,2] †, Qingliang Liao[1,2] †, Xiankun Zhang[1,2], Junli Du[1,2], Yang Ou[1,2], Jiankun Xiao[1,2], Zhuo Kang[1,2], Zheng Zhang[1,2] * and Yue Zhang[1,2] *

[1] Beijing Advanced Innovation Center for Materials Genome Engineering, Beijing Key Laboratory for Advanced Energy Materials and Technologies, University of Science and Technology Beijing, Beijing 100083, People's Republic of China.

[2] State Key Laboratory for Advanced Metals and Materials, School of Materials Science and Engineering, University of Science and Technology Beijing, Beijing 100083, People's Republic of China

†These authors contributed equally to this work.

E-mail: yuezhang@ustb.edu.cn; zhangzheng@ustb.edu.cn

ABSTRACT

Van der Waals (vdWs) heterostructures have provided a platform for nanoscale material integrations and enabled promise for use in optoelectronic devices. Due to the ultra-strength of two-dimensional materials, strain engineering is considered as an effective way to tune their band structures and further tailor the interface performance of vdWs heterostructures. However, the less-constrained vdWs interfaces make the traditional strain technique *via* lattice-mismatched growth infeasible. Here, we report a strategy to construct mixed-dimensional heterostructure arrays with periodically strain-engineered vdWs interfaces utilizing one-dimensional semiconductor-induced nanoindentation. Using monolayer MoS_2 (1L-MoS_2)/ZnO heterostructure arrays as a model system, we demonstrate inhomogeneous built-in strain gradient at the heterointerfaces ranging from 0 to 0.6% tensile. Through systematic optical characterization of the hybrid structures, we verify that strain can improve the interfacial charge transfer efficiency. Consequently, we observe that the photoluminescence (PL) emission of 1L-MoS_2 at strained interfaces is dramatically quenched more than 50% with respect to that at unstrained interfaces. Furthermore, we confirm the strain-optimized interfacial carrier behavior is attributed to the reduction of interfacial barrier height, which is originated from the strain-dependent Fermi level of 1L-MoS_2. These results demonstrate that strain provides another degree of freedom in tuning the vdWs interface performance and our method developed here should enable flexibility in achieving more sophisticated vdWs integration *via* strain engineering.

KEYWORDS: van der Waals interfaces, mixed-dimensional heterostructure arrays, strain engineering, interfacial charge transfer, photoluminescence quenching, band alignment.

Atomically thin two-dimensional (2D) materials have been the focus of materials science for fundamental researches and future technologies owing to their unique properties.[1-4] In particular, the dangling-bond-free surfaces of 2D materials offer flexibility in integrating different dimensioned materials into mixed-dimensional van der Waals (vdWs) heterostructures for next-generation electronic/optoelectronic devices.[5-8] The efficient interfacial charge-transport is crucial for high-performance heterostructures-based optoelectronic devices, such as photodetectors with ultrafast interfacial charge transfer[9, 10] and photovoltaic cells with highly efficient carriers separation.[11, 12] However, the complex, less-constrained, and more environmentally vulnerable interfaces in a vdWs heterojunction is different from that of a conventional, epitaxially grown heterojunction, engendering challenges for achieving efficient interfacial charge-transport.[13, 14] Especially, the minimal electronic hybridization across vdWs gaps requires more favorable band alignments to provide the driving force for effective charge transfer.[15, 16] As is known to all, the band offsets of vdWs heterostructures are mainly determined by the band structures of composed materials.[17, 18] Therefore, a strategy toward significantly modifying band structures of 2D materials is highly desirable for optimizing the band alignment and ultimately achieving high-performance vdWs optoelectronic devices.

Strain engineering[14, 19-21] is considered as a more stable and controllable method to tune band structures of materials compared to chemical doping or surface modification,[22, 23] which has been widely used in traditional semiconductor materials' manufacturing.[24] Furthermore, outstanding mechanical properties of 2D materials[25, 26] and considerable modulation of their electronic structures under strain[27-29] offer intriguing possibilities to achieve significant interfacial charge-transport *via* strain engineering. Traditionally, strain-engineered heterostructures are achieved by controlling lattice-mismatched growth.[30, 31] However, the intrinsically less-constrained interfaces of vdWs heterostructures make this established technique invalid. Furthermore, although mechanical bending or stretching on the flexible substrate is a

widely employed approach to achieve strain engineering on 2D materials,[32-34] this method is incapable of applying strain at the nanoscale precisely, which limits the strain-engineered vdWs integration with high-density for practical applications. Therefore, it remains a big challenge to construct vdWs heterostructures with precisely and controllably nanostrain-engineered interfaces for ultradense integration.

Here, we demonstrate an effective method to apply strain on vdWs interfaces by one-dimensional semiconductor-tailored nanoindentation during the wet transfer process. With the advantage of highly controllable homoepitaxial-growth at low temperature,[35, 36] ZnO semiconductor nanorod arrays (NRAs) provide an essential nanopatterned structure for constructing monolayer MoS_2 (1L-MoS_2)/ZnO nanorod heterostructure arrays with periodically strain-engineered interfaces. In this model system, the strain-tailored interfaces dramatically suppress the photoluminescence emission of 1L-MoS_2 and highly enhance the interfacial charge transfer efficiency. Furthermore, we demonstrate the optimized interfacial carrier behaviors are attributed to the formation of a more favorable band alignment under strain modulation.

RESULTS AND DISCUSSION

The fabrication process and schematic diagrams of the periodic strained 1L-MoS_2/ZnO nanorod mixed-dimensional vdWs heterostructure arrays are depicted in Figure 1a and 1b. Firstly, the single crystal ZnO substrates were patterned *via* electron beam lithography.[37, 38] The patterned ZnO NRAs were homo-epitaxially grown on the ZnO substrates with perfect c-axis orientations by hydrothermal synthesis. Secondly, the as-grown 1L-MoS_2 was accurately transferred onto ZnO NRAs using a poly (methyl methacrylate) (PMMA)-assisted wet transfer method.[39] The basic characterizations of ZnO NRAs and 1L-MoS_2 are shown in Supporting Information, Figures S1. Then, the capillary force originated from water evaporation between adjacent ZnO nanorods pulled down PMMA-protected 1L-MoS_2. In this process, each ZnO nanorod applied nanoindentation (biaxial strain) to 1L-MoS_2. Controlling the rate of water evaporation in this process is a crucial step to obtain well-defined heterostructure arrays (Supporting Information, Figures S2). Finally, the hybrid structures were immersed in acetone to remove PMMA and dried in a critical point dryer to remove acetone.[40, 41] Notablely, utilizing patterned substrates to locally apply strain on 2D materials has been carried out in previous reports,[41-45] which mainly focus on the fundamental properties of strained 2D materials. However, in this study, we constructed strain-engineered vdWs heterointerfaces with bottom-up designed one-dimensional semiconductor nanomaterials and explored the carriers transport behaviors at the strain-modulated heterointerfaces. Besides, the construction of strain-modulated vdWs heterostructures is different from simply applying strain on 2D materials. During this process, it is necessary not only to apply strain effectively but also to construct strong coupling heterointerfaces. Therefore, we employed a mild annealing strategy (Supporting Information, Figure S3) to avoid the unintentional influence of the residual water at the interfaces and reduce the vdWs gap.

The morphology of the heterostructure arrays was characterized by the scanning electron microscopy (SEM) (Figure 1c). The organized wrinkles of MoS_2 can be seen

clearly connecting the two adjacent ZnO nanorods, suggesting the existence of periodic deformation in 1L-MoS_2, which will be verified in later. The similar feature was also observed by atomic force microscopy (AFM) (Figure 1d). The height of the ZnO NRAs is about 260 nm. The MoS_2/ZnO heterostructure arrays were also verified by the Raman scattering (Figure 1e). The vibrational modes of E_2^{low} (99 cm^{-1}) and E_2^{high} (438 cm^{-1}) demonstrate the presence of ZnO.[46] Besides, the gaps between the in-plane mode (E^1_{2g}) at 385 cm^{-1} and out-of-plane mode (A_{1g}) at 403 cm^{-1} are 18 cm^{-1}, which signifies the existence of 1L-MoS_2.[47]

Since the shift on the Raman modes upon applied strain can be employed to quantify the strain distributions,[48, 49] the confocal Raman measurements were carried out with an excitation wavelength of 532 nm (2.33 eV). The distribution mappings for the E^1_{2g} peak frequencies of 1L-MoS_2 on (4 × 4) ZnO NRAs is shown in Figure 2a. The E^1_{2g} peak position of 1L-MoS_2 on the top of each ZnO nanorod is red-shifted, which indicates that periodically localized biaxial-strain at the nanoscale (determined by the diameter of ZnO nanorods) was applied on the 1L-MoS_2.[49, 50] That means the 1L-MoS_2/ZnO heterostructure arrays with nanostrain-engineered heterointerfaces were successfully achieved. We note that we also exclude the temperature and geometry factors on the Raman shift of strained 1L-MoS_2 (Supporting Information, Figures S4). In order to avoid the unintentional heating of the 1L-MoS_2 by laser, we limited the laser power below 200 μw for Raman measurements.

To further accurately analyze the strain distribution by the 500-nm diameter laser beam, we chose a ZnO nanorod with the diameter over 2 μm (Figure 2b). According to the position of 1L-MoS_2, the 1L-MoS_2 can be divided into three different regions: A (on the flat ZnO substrate), B (on the top edge of the ZnO nanorod) and C (on the top of the ZnO nanorod). Figure 2c and 2d show the frequency mappings for the E^1_{2g} and A_{1g} peak of 1L-MoS_2 on the single ZnO nanorod, respectively. In fact, the larger red-shift of the E^1_{2g} peak position and the slighter red-shift of the A_{1g} peak position observed on the strained 1L-MoS_2 are in good agreement with recent studies about the tensile

biaxial-strain effects on the Raman spectrum of 1L-MoS_2.[29, 42] The typical Raman spectra in different regions (A, B and C) were extracted from the Raman mapping spectrum (Figure 2e). Compared with the 1L-MoS_2 in region C, the 1L-MoS_2 in region A and B are obviously red-shifted for both E^1_{2g} and A_{1g} peaks: 1.5 cm^{-1} and 0.5 cm^{-1} for region A and 3 cm^{-1} and 1 cm^{-1} for region B. According to the red-shift magnitudes of in-plane mode (E^1_{2g}) in different regions, we can determine that most-strained region is B, the strained region is A, and the almost unstrained region is C (Figure 2f). Therefore, the spatially strained vdWs heterointerfaces were distributed on the top of ZnO nanorods. Furthermore, the strain-dependent E^1_{2g} Raman mode enables us to estimate the applied biaxial-strain on 1L-MoS_2. In general, there are two formulas about calculating the strain based on the Raman shifts. The first formula is $\varepsilon = \frac{\Delta\omega}{\chi}$, in which χ is the shift rates of Raman vibrational modes. According to previous reports, the shift rates of E^1_{2g} mode under biaxial strain is ~5.2 cm^{-1} per % strain.[29, 42] Therefore, based on this formula, the max biaxial strain in our experiments is about 0.6 %. The second formula is $\varepsilon = \frac{\Delta\omega}{2\gamma\omega_0}$ for the biaxial strain,[29, 51] in which γ is the Grüneisen parameter. The fitted γ of E^1_{2g} mode of 1L-MoS_2 is 0.6-0.65.[48, 49] Based on the second formula, the calculated max biaxial tensile strain is ε_{max} = 0.6-0.7%. After double checking the calculated results of biaxial tensile strain based on these two formulas, we have demonstrated the most applied biaxial-strain (ε_{max}) on 1L-MoS_2 is ≈ 0.6%.

To directly study strain effects on the interfacial carrier behaviors of 1L-MoS_2/ZnO heterostructure arrays (Figure 3a), comprehensive PL measurements were performed under 532 nm (~2.33 eV) laser excitation. We first verified the existence of the charge transfer between (unstrained) 1L-MoS_2 and ZnO. 20 nm Al_2O_3 was deposited on the ZnO substrate by atomic layer deposition (ALD). 1L-MoS_2 was transferred onto the boundary between Al_2O_3 and ZnO. Compared with the 1L-MoS_2 on Al_2O_3, the PL intensity of 1L-MoS_2 is quenched in the heterostructure area (under 532 nm laser excitation), as shown in Figure 3a. It should be noted that the epitaxial-grown ZnO NRAs were similar to the ZnO substrates and both of them can not produce significant

emission under 532 nm laser excitation (Supporting Information, Figure S5). Meanwhile, PL measurements for ZnO were also performed utilizing 325 nm laser. ZnO shows a strong ultraviolet emission peak at ~3.37 eV. Specifically, the PL intensity of ZnO in the overlap area was also suppressed with respect to pristine ZnO (Figure 3b), indicating that ZnO and 1L-MoS_2 form a type-II band alignment for efficient charge transfer. To systematically analyze the mechanism of charge transfer at the 1L-MoS_2/ZnO interfaces, each PL spectra of 1L-MoS_2 on the Al_2O_3 (top) and 1L-MoS_2 on the 1L-MoS_2 on the ZnO (bottom) was decomposed by the B exciton (∼1.97 eV), neutral exciton (A^o, ~1.83 eV) and trion (A^T, ∼1.78 eV) (Figure 3c), using Lorentzian fitting functions.[52, 53] We found that upon forming the heterostructure (1L-MoS_2/ZnO), the spectral weight of A^o increased, while that of the trion decreased.[39, 54] We also measured the power-dependent PL using a wide range of laser powers (0.005−5 mW) (Figure 3d). As the excitation laser power is increased, the major emission of the pristine 1L-MoS_2 (on the Al_2O_3) is dominated by A^T. In contrast, the major PL emission of 1L-MoS_2 in the heterostructure is dominated by A^o. Trion excitons are almost depleted during charge transfer. As a result, we confirm that the PL intensity of 1L-MoS_2 on ZnO is closely related to the charge transfer between 1L-MoS_2 and ZnO.

Furthermore, to reveal the strain effects on the interfacial carrier behaviors of the heterostructure arrays, different built-in electrical field contributions on PL emission of 1L-MoS_2 should be considered. There is not only a built-in field originated from the band offset of 1L-MoS_2/ZnO, but also a built-in field in 1L-MoS_2 induced by strain gradient. Both of them can modulate the carrier behaviors of 1L-MoS_2, which will have impacts on the PL emission of 1L-MoS_2. To separate two contributions on the PL intensity of 1L-MoS_2, 10 nm insulating layer (Al_2O_3) was deposited on the surface of ZnO NRAs using ALD. Then 1L-MoS_2 was transferred in a similar way to form MoS_2/Al_2O_3/ZnO hybrid structures (Figure 4a). Due to blocking the interaction between 1L-MoS_2 and ZnO, the PL intensity of strained 1L-MoS_2 was only related to the built-in field induced by the strain gradient in 1L-MoS_2. From the PL intensity

mapping of 1L-MoS_2 on Al_2O_3/ZnO (integrated intensity from 1.75 eV -1.85 eV) (Figure 4b), the strained 1L-MoS_2 shows a 1.5 times higher PL intensity than the unstrained 1L-MoS_2. By comparing the typical PL signals of 1L-MoS_2 taken from the region A and region B (Figure 4c), we found that the strained 1L-MoS_2 (region B) exhibits a red-shift of A-exciton: 55 meV in comparison with unstrained 1L-MoS_2 (region A). The reduced optical band gap is the result of the biaxial tensile strain, which has been demonstrated in previous reports[32, 42]. More interestingly, the enhanced PL intensity of MoS_2 on the Al_2O_3/ZnO NRAs is originated from the quantum confinement of excitons due to built-in field induced by the strain gradient (Figure 4g),[32] which demonstrates our hybrid structures have great potentials in achieving arrays of quantum emitters based on transition metal dichalcogenides with strong PL emission (such as WSe_2, WS_2).[43, 45] In a word, the built-in field induced by strain gradient can dramatically enhance the PL intensity of 1L-MoS_2 on Al_2O_3/ZnO NRAs.

Finally, we carried out PL measurements for 1L-MoS_2 on ZnO (Figure 4d). From the PL mapping in Figure 4e, the dramatically decreased PL signal of 1L-MoS_2 was observed at strain-concentrated interfaces. According to the typical PL spectra of 1L-MoS_2 in a different region (C and D) (Figure 4f), the A exciton peak of strained 1L-MoS_2 on ZnO shows the similar red-shift (50 meV) with strained 1L-MoS_2 on Al_2O_3/ZnO. However, the PL intensity of strained 1L-MoS_2 decreased more than 50% compared with that of unstrained 1L-MoS_2. The decreased PL signal of strained 1L-MoS_2 on ZnO was completely different from our observation of strained 1L-MoS_2 on Al_2O_3/ZnO. Therefore, we ruled out the contribution (strain-induced built-in field in 1L-MoS_2) on the decreased PL intensity of 1L-MoS_2 on ZnO. We note that the decreased PL intensity of strained 1L-MoS_2 (at the center of the 1L-MoS_2 crystal) was not originated from the nucleus of 1L-MoS_2 (Supporting Information, Figure S6).[55] We also performed PL intensity mapping of 1L-MoS_2 on the boundary between the ZnO substrates and the ZnO NRAs (Figure 4h). The PL intensity of 1L-MoS_2 on the ZnO substrates (unstrained 1L-MoS_2) was uniform. However, the PL intensity of 1L-MoS_2

on the ZnO NRAs (strained 1L-MoS_2) varified spatially. The lower PL intensity appears centrally on the top of ZnO nanorods (strained 1L-MoS_2), while higher PL intensity appears between ZnO nanorods (unstrained 1L-MoS_2), which further verifies periodic strain-dependent PL intensity of 1L-MoS_2 on ZnO. We exclude the strain-induced direct to indirect bandgap transition[40, 56] in 1L-MoS_2 due to the limited biaxial strain (<1%) in our experiments. Besides, we discuss the geometry factor on the PL intensity of periodic strained 1L-MoS_2 (Supporting Information, Figure S7) and eliminate their influences by the mild annealing strategy that has been described in Supporting Information, Figure S3. As a result, we ruled out alternate factors discussed above and attributed the decreased PL signal of strained 1L-MoS_2 on ZnO to the strain-engineered heterointerfaces. Considering the existence of charge transfer between ZnO and 1L-MoS_2, the anomalous decreased PL emission was mainly originated from the more efficient separation of photogenerated carriers at the strain-tailored heterointerfaces (Figure 4i).

As is known to all, the interfacial carrier behaviors are determined by the band alignment of heterostructures.[57] To better understand the origin of enhanced charge transfer efficiency at strained heterointerfaces, the band alignment of 1L-MoS_2/ZnO was analyzed using ultraviolet photoelectron spectroscopy (UPS) measurements.[18, 39] The work function can be calculated from the difference between the cut off of the highest binding energy and the photon energy of the exciting radiation. The work function of ZnO and 1L-MoS_2 are calculated as 4.19 eV and 4.51 eV (Figure 5a), respectively. Besides, the energy difference between the valence band maximum (VBM) and Fermi level of MoS_2 is 1.68 eV. Meanwhile, the distance of the VBM to the Fermi level of ZnO is 2.91 eV (in a flat band condition) (Figure 5b). When the 1L-MoS_2/ZnO heterojunction is formed, electrons in the ZnO diffuse into the 1L-MoS_2 at the junction area to balance the different Fermi levels, which results in the band bending of ZnO at the interface. This band bending corresponds to an accumulation of negative charge at the ZnO surface, compensated by an opposite positive charge inside the semiconductor

(depletion layer).[58] Considering the different work function between MoS_2 and ZnO, an upward band bending (V_{BB}) of about 0.32 eV is present at the ZnO (0001) surface. Moreover, we determined a value of 3.37 eV for the ZnO optical gap at room temperature by PL measurements. According to the exciton binding energy of ZnO about 60 meV,[59] we deduced a ZnO excitonic gap about 3.43 eV. Based on the reported quasi-particle band structure of 1L-MoS_2 using scanning tunneling microscopy, the band gap of 1L-MoS_2 is 2.4 eV,[60] which is larger than the optical band gap (1.83 eV) considering the large binding energy for the excitons in MoS_2. On the basis of the above results, we constructed a band diagram showing the quasi-type II band alignment at the 1L-MoS_2 and ZnO interface, as depicted in Figure 5c. The conduction band discontinuity ΔE_C is calculated from $\Delta E_C = \Delta E_V - V_{BB} - (E_{1L\text{-}MoS2} - E_{ZnO})$, in which $E_{1L\text{-}MoS2}$ and E_{ZnO} are the bandgap energies of 1L-MoS_2 and ZnO, respectively. We obtained ΔE_C = -0.13 eV. The conduction offset is also the peak barrier between 1L-MoS_2 and ZnO. In order to drift into ZnO, the photo-generated electrons in 1L-MoS_2 have to overcome the peak barrier with high energy or tunnel through the barrier. The height of peak barrier plays an essential role in the charge transfer efficiency between 1L-MoS_2 and ZnO, which will be discussed in detail later.

The band structure of 1L-MoS_2 under biaxial strain was analyzed by first-principles density functional theory (DFT) calculations.[27] It should be noted that we limit the calculated biaxial strain to 1% to prevent 1L-MoS_2 from the indirect band gap transition. The strain-dependent bandgap energy levels for an electron and hole at the K point in the first Brillouin zone are shown in Figure 5d. The calculation results indicate that the direct bandgap of 1L-MoS_2 reduces and both of the electron and hole level decrease with increasing strain. More importantly, the Fermi level of 1L-MoS_2 is shifted up under the tensile strain, which was consistent with the previous report.[34, 61] In order to double-check the change of Fermi level under strain, we further performed Kelvin probe force microscopy (KPFM) measurements to gain insight into the work function of MoS_2 (strained and unstrained MoS_2) and ZnO.[62-64] The KPFM image displays a

clear surface potential contrast between unstrained 1L-MoS_2 and ZnO (Figure 5e). From the potential profile across the edge of unstrained MoS_2/ZnO, we obtained a surface potential difference of ≈ 280 mV between ZnO and unstrained 1L-MoS_2 (Figure 5f). The sample surface potential can be obtained by $\varphi_{tip} - \varphi_{sample} = e\ V_{sp}$, where φ_{tip} and φ_{sample} are the work functions of the conductive tip and sample, respectively, and V_{sp} is the measured surface potential. Therefore, the obtained work function of ZnO is ~280 meV lower than unstrained 1L-MoS_2, which matches well with the results obtained from the UPS measurements. More importantly, compared with unstrained MoS_2, the work function of strained 1L-MoS_2 decreases 80 meV. That means the Fermi level of MoS_2 is shifted up under biaxial tensile strain, which is consistent with theory calculation.

Finally, according to the measured band structures and theory calculations, energy band diagrams are introduced to understand the observed phenomena and elucidate the mechanism of strain effects on the band alignment of ZnO/MoS_2. As shown in Figure 5h, the peak barrier at the conduction band of the interface decreases the rate of the photogenerated electron transfer from 1L-MoS_2 to ZnO, which means the peak barrier dominates the interfacial carrier behaviors. Compared with the pristine MoS_2, the Fermi level of tensile biaxial-strained MoS_2 is shifted up (Figure 5g), which lowers the built-in field at the interface and results in the reduction of band bending of ZnO. Even though the CBM also decreases under strain, the degree of the shifted Fermi level (~80 meV measured from KPFM in Figure 5f) is larger than the degree of the decline of CBM (~50 meV obtained from PL spectra in Figure 5c). As a consequence, the peak barrier height between strained MoS_2 and ZnO decreases with respect to unstrained MoS_2 and ZnO (Figure 5i). The photoexcited electrons that transfer from strained 1L-MoS_2 to ZnO can be promoted more effectively and the recombination of electron-hole in 1L-MoS_2 is further suppressed, leading to the dramatic PL quenching of 1L-MoS_2 at the strained interfaces. In short, these above results indicate that strain is able to function as another degree of freedom in vdWs heterostructures to modulate the charge

transfer efficiency, which potentially provides a strategy to optimize the performance of optoelectronic based on vdWs heterostructures. Meanwhile, the strain effects that control the interfacial band alignment give rise to the observed carrier behaviors modulation.

CONCLUSIONS

In summary, we propose an effective method to construct vdWs heterostructure arrays with nanostrain-engineered interfaces. The periodically gradient biaxial-strain can be applied by patterned one-dimensional semiconductor-induced nanoindentation. Using ZnO and MoS_2 a model system, we verify that the strain-engineered interfaces can effectively tune the band alignment of MoS_2/ZnO and optimize the interfacial carrier behaviors for more efficient charge transfer, indicating the great potential of strain engineering on modulating vdWs interfacial carrier behaviors for high-performance optoelectronic devices. By expanding on this method, it may be possible to design vertical vdWs heterostructures-based photodetectors and photovoltaics with high-density integration *via* strain engineering.

METHODS

Preparation of the monolayer MoS_2. The monolayer MoS_2 was prepared by chemical vapor deposition (CVD). Molybdenum trioxide (MoO_3, Sigma-Aldrich, ≥99.5% purity) and sulfur (S, Sigma-Aldrich, ≥99.5% purity) powder were used as sources. 10 mg MoO_3 powder was loaded in a quartz boat. A piece of Si wafer capped with 300 nm SiO_2 layer was suspended on the quartz boat with the polished side facing down. Then the quartz boat was located at the center of a quartz tube furnace. A ceramic boat containing S powder (3 g) was placed at an upstream position where the temperature would reach 180 ºC during the growth. The tube was purged with 300 sccm argon (Ar) gas for 10 min at 300 ºC temperature, then heated to 850 ºC within 15 min. And the temperature maintained at 850 ºC for 30 min with oxygen (O_2) assist of 2 sccm. The system was then allowed to cool down to room temperature naturally.

Synthesis of patterned ZnO nanorod arrays. For epitaxial growth of patterned

ZnO NRAs, the c-oriented single-crystalline ZnO substrates were used directly. The negative photoresist (PR) (AR-N 950K) was spin-coated on the substrates at 3000 rpm/min for 50 s to form PR films with a thickness of 300 nm. which was followed by a baking process at 180 ºC on a hotplate for 1 min. Then, the tunable arrangement and period of the template were designed *via* e-beam lithography. Finally, the patterned ZnO NRAs were synthesized in a 200 mL aqueous solution of equimolar (0.05 mol/L) zinc nitrate and hexamethylenetetramine (HMTA), with the template substrates upside down at 95 ºC for 3 h. After the solution cooled down, the substrates were taken out and cleaned by soaked in acetone for 30 min to remove PR. And the samples were washed with deionized water and dried in an oven at 60 ºC for 10 min. The selected monolayer MoS_2 was transferred onto the ZnO nanorod arrays with the help of accurate transfer platform (Metatest, E1-T).

Measurements. The morphology of ZnO NRAs and MoS_2/ZnO heterostructures were characterized by scanning electron microscopy(SEM) (Quanta 3D, FEI). The crystallography of the ZnO NRAs was obtained by transmission electron microscopy (TEM) (TECNAI, F20). The AFM images and KPFM measurements were taken on a commercially available AFM (Nanoscope IIID, Multimode). The PL and Raman spectrum measurements of MoS_2 were performed with the excitation laser line of 532 nm using a WITEC alpha500 Confocal Raman system in the ambient air environment. The power of the excitation laser line was kept below 5 mW to avoid damage of MoS_2. The Raman scattering was collected by an Olympus 100 × objective (N.A.=0.9) and dispersed by 1800 (for Raman measurements) and 600 (for PL measurements) lines per mm gratings. The PL spectra of ZnO under 325 nm excitation was obtained by confocal microscopy (JY-HR800) with a power of 0.5 mW. UPS curves were obtained in an ultrahigh vacuum chamber using a helium lamp source emitting (AXIS ULTRA DLD) at 21.2 eV.

Theory calculation of band structure of monolayer MoS_2 under tensile biaxial-strain. The numerical calculation was performed in the Vienna *ab initio* simulation

package (VASP) within the framework of the projected augment wave method. The exchange correlation density functional is represented in the form of Perdew Burke Ernzerhof (PBE), base on generalized gradient approximation. Spin-orbital interaction is included. The cutoff energy of the plane wave is 600 eV. The first Brillouin zone is sampled on a $24 \times 24 \times 1$ Γ centered K-space mesh. We chose 10^{-6} eV as the criterion of electron self-consist iteration. An over 18 Å height vacuum is used to avoid the interlayer interaction due to periodic boundary condition.

ASSOCIATED CONTENT

The Supporting Information is available free of charge on the ACS Publications website at DOI: XXXX.

Additional information includes: Basic materials characterizations (S1); SEM images of strained heterostructure arrays with different water evaporation rates(S2); The mild annealing strategy for strong-coupling heterointerfaces (S3); Temperature and geometry factors on the Raman shift of 1L-MoS_2 (S4); PL and Raman measurements of ZnO nanorod arrays under 532 nm laser excitation (S5); The geometry factor on the PL intensity of 1L-MoS_2 on the ZnO nanorod (S6); Scanning PL maps of as-grown 1L-MoS_2 and part of 1L-MoS_2 on the Al_2O_3 coated ZnO nanorod (S7).

The authors declare no conflict of interest.

AUTHOR INFORMATION

Corresponding Authors

*E-mail: yuezhang@ustb.edu.cn

*E-mail: zhangzheng@ustb.edu.cn

ORCID

Baishan Liu: 0000-0003-3738-1874

Xiankun Zhang: 0000-0001-9654-4659

Zheng Zhang: 0000-0002-9104-7562

Yue Zhang: 0000-0002-8213-1420

Author contributions

B.S.L., Z.Z. and Y.Z. designed the experiments. B.S.L. performed device fabrication and optical measurements. X.K.Z. performed TEM, UPS measurements. J.L.D. assisted in the AFM measurements and patterned ZnO growth. Y.O. carried out the theory calculation. J.K.X. synthesized monolayer MoS_2 by CVD. B.S.L., Q.L.L., Z.K., Z.Z. and Y.Z. wrote the manuscript, and all authors discussed the results and commented on the manuscript. B.S.L. and Q.L.L. contributed equally.

ACKNOWLEDGMENTS

This work was supported by the National Natural Science Foundation of China (No. 51527802, 51602020, 51722203, and 51672026), the Overseas Expertise Introduction Projects for Discipline Innovation (No. B14003), the National Key Research and Development Program of China (No. 2016YFA0202701), the Beijing Municipal Science & Technology Commission (Z161100002116027), the Fundamental Research Funds for the Central Universities (FRF-TP-18-001C1, FRF-BD-18-012A).

REFERENCES

1. Novoselov, K. S.; Geim, A. K.; Morozov, S. V.; Jiang, D.; Zhang, Y.; Dubonos, S. V.; Grigorieva, I. V.; Firsov, A. A. Electric Field Effect in Atomically Thin Carbon Films. *Science* **2004**, *306*, 666-669.
2. Mak, K. F.; Lee, C.; Hone, J.; Shan, J.; Heinz, T. F. Atomically Thin MoS_2: A New Direct-Gap Semiconductor. *Phys. Rev. Lett.* **2010**, *105*, 136805.
3. Liu, H.; Neal, A. T.; Zhu, Z.; Luo, Z.; Xu, X.; Tománek, D.; Ye, P. D. Phosphorene: An Unexplored 2D Semiconductor with a High Hole Mobility. *ACS Nano* **2014**, *8*, 4033-4041.
4. Tao, L.; Cinquanta, E.; Chiappe, D.; Grazianetti, C.; Fanciulli, M.; Dubey, M.; Molle, A.; Akinwande, D. Silicene Field-Effect Transistors Operating at Room Temperature. *Nat. Nanotechnol.* **2015**, *10*, 227-231.
5. Novoselov, K. S.; Castro Neto, A. H. Two-Dimensional Crystals-Based Heterostructures: Materials with Tailored Properties. *Phys. Scr.* **2012**, *2012*, 014006.
6. Novoselov, K.; Mishchenko, A.; Carvalho, A.; Neto, A. C. 2D Materials and van der Waals Heterostructures. *Science* **2016**, *353*, aac9439.
7. Liu, Y.; Weiss, N. O.; Duan, X.; Cheng, H.-C.; Huang, Y.; Duan, X. Van der Waals Heterostructures and Devices. *Nat. Rev. Mater.* **2016**, *1*, 16042.
8. Liu, C.; Yan, X.; Song, X.; Ding, S.; Zhang, D. W.; Zhou, P. A Semi-Floating Gate Memory Based on van der Waals Heterostructures for Quasi-Non-Volatile Applications. *Nat. Nanotechnol.* **2018**, *13*, 404-410.
9. Mao, J.; Yu, Y.; Wang, L.; Zhang, X.; Wang, Y.; Shao, Z.; Jie, J. Ultrafast, Broadband Photodetector Based on $MoSe_2$/Silicon Heterojunction with Vertically Standing Layered Structure Using Graphene as Transparent Electrode. *Adv. Sci.* **2016**, *3*, 1600018.
10. Bullock, J.; Amani, M.; Cho, J.; Chen, Y.-Z.; Ahn, G. H.; Adinolfi, V.; Shrestha, V. R.; Gao, Y.; Crozier, K. B.; Chueh, Y.-L. Polarization-Resolved Black Phosphorus/Molybdenum Disulfide Mid-Wave Infrared Photodiodes with High

Detectivity at Room Temperature. *Nat. Photonics* **2018**, *12*, 601-607.

11. Tsai, M.-L.; Su, S.-H.; Chang, J.-K.; Tsai, D.-S.; Chen, C.-H.; Wu, C.-I.; Li, L.-J.; Chen, L.-J.; He, J.-H. Monolayer MoS_2 Heterojunction Solar Cells. *ACS Nano* **2014**, *8*, 8317-8322.
12. Song, Y.; Li, X.; Mackin, C.; Zhang, X.; Fang, W.; Palacios, T. s.; Zhu, H.; Kong, J. Role of Interfacial Oxide in High-Efficiency Graphene–Silicon Schottky Barrier Solar Cells. *Nano Lett.* **2015**, *15*, 2104-2110.
13. Liu, X.; Hersam, M. C. Interface Characterization and Control of 2D Materials and Heterostructures. *Adv. Mater.* **2018**, *30*, 1801586.
14. Dai, Z.; Liu, L.; Zhang, Z. Strain Engineering of 2D Materials: Issues and Opportunities at the Interface. *Adv. Mater.* **2019**, 1805417.
15. Hong, X.; Kim, J.; Shi, S. F.; Zhang, Y.; Jin, C.; Sun, Y.; Tongay, S.; Wu, J.; Zhang, Y.; Wang, F. Ultrafast Charge Transfer in Atomically Thin MoS_2/WS_2 Heterostructures. *Nat. Nanotechnol.* **2014**, *9*, 682-686.
16. Lee, C. H.; Lee, G. H.; Zande, A. M. V. D.; Chen, W.; Li, Y.; Han, M.; Cui, X.; Arefe, G.; Nuckolls, C.; Heinz, T. F. Atomically Thin *p-n* Junctions with van der Waals Heterointerfaces. *Nat. Nanotechnol.* **2014**, *9*, 676-681.
17. Chiu, M.-H.; Zhang, C.; Shiu, H.-W.; Chuu, C.-P.; Chen, C.-H.; Chang, C.-Y. S.; Chen, C.-H.; Chou, M.-Y.; Shih, C.-K.; Li, L.-J. Determination of Band Alignment in the Single-Layer MoS_2/WSe_2 Heterojunction. *Nat. Commun.* **2015**, *6*, 7666.
18. Wu, H.; Kang, Z.; Zhang, Z.; Zhang, Z.; Si, H.; Liao, Q.; Zhang, S.; Wu, J.; Zhang, X.; Zhang, Y. Interfacial Charge Behavior Modulation in Perovskite Quantum Dot-Monolayer MoS_2 0D-2D Mixed-Dimensional van der Waals Heterostructures. *Adv. Funct. Mater.* **2018**, *28*, 1802015.
19. Deng, S.; Sumant, A. V.; Berry, V. Strain Engineering in Two-Dimensional Nanomaterials Beyond Graphene. *Nano Today* **2018**, *22*, 14.
20. Neto, A.; Novoselov, K. Two-Dimensional Crystals: Beyond Graphene. *Mater. Express* **2011**, *1*, 10-17.
21. Li, J.; Shan, Z.; Ma, E. Elastic Strain Engineering for Unprecedented Materials

Properties. *MRS Bull.* **2014**, *39*, 108-114.

22. Lei, S.; Wang, X.; Li, B.; Kang, J.; He, Y.; George, A.; Ge, L.; Gong, Y.; Dong, P.; Jin, Z. Surface Functionalization of Two-Dimensional Metal Chalcogenides by Lewis Acid–Base Chemistry. *Nat. Nanotechnol.* **2016**, *11*, 465-471.
23. Huo, N.; Konstantatos, G. Ultrasensitive All-2D MoS_2 Phototransistors Enabled by an out-of-Plane MoS_2 PN Homojunction. *Nat. Commun.* **2017**, *8*, 572.
24. Thompson, S. E.; Armstrong, M.; Auth, C.; Alavi, M.; Buehler, M.; Chau, R.; Cea, S.; Ghani, T.; Glass, G.; Hoffman, T. A 90-nm Logic Technology Featuring Strained-Silicon. *IEEE Trans. Electron Devices* **2004**, *51*, 1790-1797.
25. Lee, C.; Wei, X.; Kysar, J. W.; Hone, J. Measurement of the Elastic Properties and Intrinsic Strength of Monolayer Graphene. *Science* **2008**, *321*, 385-388.
26. Bertolazzi, S.; Brivio, J.; Kis, A. Stretching and Breaking of Ultrathin MoS_2. *ACS Nano* **2011**, *5*, 9703-9709.
27. Feng, J.; Qian, X.; Huang, C.-W.; Li, J. Strain-Engineered Artificial Atom as a Broad-Spectrum Solar Energy Funnel. *Nat. Photonics* **2012**, *6*, 866-872.
28. Desai, S. B.; Seol, G.; Kang, J. S.; Fang, H.; Battaglia, C.; Kapadia, R.; Ager, J. W.; Guo, J.; Javey, A. Strain-Induced Indirect to Direct Bandgap Transition in Multilayer WSe_2. *Nano Lett.* **2014**, *14*, 4592-4597.
29. Lloyd, D.; Liu, X.; Christopher, J. W.; Cantley, L.; Wadehra, A.; Kim, B. L.; Goldberg, B. B.; Swan, A. K.; Bunch, J. S. Band Gap Engineering with Ultralarge Biaxial Strains in Suspended Monolayer MoS_2. *Nano Lett.* **2016**, *16*, 5836-5841.
30. Stringfellow, G. The Importance of Lattice Mismatch in the Growth of $Ga_xIn_{1-x}P$ Epitaxial Crystals. *J. Appl. Phys.* **1972**, *43*, 3455-3460.
31. Jifeng, L.; Xiaochen, S.; Dong, P.; Xiaoxin, W.; Kimerling, L. C.; Koch, T. L.; Jurgen, M. Tensile-Strained, *n*-Type Ge as a Gain Medium for Monolithic Laser Integration on Si. *Opt. Express* **2007**, *15*, 11272.
32. Castellanos-Gomez, A.; Roldán, R.; Cappelluti, E.; Buscema, M.; Guinea, F.; Zant, H. S. J. V. D.; Steele, G. A. Local Strain Engineering in Atomically Thin MoS_2. *Nano Lett.* **2013**, *13*, 5361-5366.

33. Zhang, Z.; Li, L.; Horng, J.; Wang, N. Z.; Yang, F.; Yu, Y.; Zhang, Y.; Chen, G.; Watanabe, K.; Taniguchi, T. Strain-Modulated Bandgap and Piezo-Resistive Effect in Black Phosphorus Field-Effect Transistors. *Nano Lett.* **2017**, *17*, 6097-6103.

34. Sarwat, S. G.; Tweedie, M.; Porter, B. F.; Zhou, Y.; Sheng, Y.; Mol, J. A.; Warner, J. H.; Bhaskaran, H. Revealing Strain Induced Effects in Ultrathin Heterostructures at the Nanoscale. *Nano Lett.* **2018**, *18*, 2467-2474.

35. Zhang, Z.; Liao, Q.; Yu, Y.; Wang, X.; Zhang, Y. Enhanced Photoresponse of ZnO Nanorods-Based Self-Powered Photodetector by Piezotronic Interface Engineering. *Nano Energy* **2014**, *9*, 237-244.

36. Greene, L. E.; Law, M.; Tan, D. H.; Montano, M.; Goldberger, J.; Somorjai, G.; Yang, P. General Route to Vertical ZnO Nanowire Arrays Using Textured ZnO Seeds. *Nano Lett.* **2005**, *5*, 1231-1236.

37. Greene, L. E.; Law, M.; Goldberger, J.; Kim, F.; Johnson, J. C.; Zhang, Y.; Saykally, R. J.; Yang, P. Low - Temperature Wafer - Scale Production of ZnO Nanowire Arrays. *Angew. Chem.* **2003**, *115*, 3139-3142.

38. Liu, S.; Liao, Q.; Lu, S.; Zhang, Z.; Zhang, G.; Zhang, Y. Strain Modulation in Graphene/ZnO Nanorod Film Schottky Junction for Enhanced Photosensing Performance. *Adv. Funct. Mater* **2016**, *26*, 1347-1353.

39. Zhang, X.; Liao, Q.; Liu, S.; Kang, Z.; Zhang, Z.; Du, J.; Li, F.; Zhang, S.; Xiao, J.; Liu, B. Poly (4-Styrenesulfonate)-Induced Sulfur Vacancy Self-Healing Strategy for Monolayer MoS_2 Homojunction Photodiode. *Nat. Commun.* **2017**, *8*, 15881.

40. Chaste, J.; Missaoui, A.; Huang, S.; Henck, H.; Ben, A. Z.; Ferlazzo, L.; Naylor, C.; Balan, A.; Jr, J. A.; Braive, R. Intrinsic Properties of Suspended MoS_2 on SiO_2/Si Pillar Arrays for Nanomechanics and Optics. *Acs Nano* **2018**, *12*, 3235-3242.

41. Reserbat-Plantey, A.; Kalita, D.; Han, Z.; Ferlazzo, L.; Autier-Laurent, S.;

Komatsu, K.; Li, C.; Weil, R.; Ralko, A.; Marty, L. Strain Superlattices and Macroscale Suspension of Graphene Induced by Corrugated Substrates. *Nano Lett.* **2014**, *14*, 5044-5051.

42. Li, H.; Contryman, A. W.; Qian, X.; Ardakani, S. M.; Gong, Y.; Wang, X.; Weisse, J. M.; Lee, C. H.; Zhao, J.; Ajayan, P. M. Optoelectronic Crystal of Artificial Atoms in Strain-Textured Molybdenum Disulphide. *Nat. Commun.* **2015**, *6*, 7381.
43. Branny, A.; Kumar, S.; Proux, R.; Gerardot, B. D. Deterministic Strain-Induced Arrays of Quantum Emitters in a Two-Dimensional Semiconductor. *Nat. Commun.* **2017**, *8*, 15053.
44. Tomori, H.; Kanda, A.; Goto, H.; Ootuka, Y.; Tsukagoshi, K.; Moriyama, S.; Watanabe, E.; Tsuya, D. Introducing Nonuniform Strain to Graphene Using Dielectric Nanopillars. *Appl. Phys. Express* **2011**, *4*, 075102.
45. Palacios-Berraquero, C.; Kara, D. M.; Montblanch, A. R.; Barbone, M.; Latawiec, P.; Yoon, D.; Ott, A. K.; Loncar, M.; Ferrari, A. C.; Atatüre, M. Large-Scale Quantum-Emitter Arrays in Atomically Thin Semiconductors. *Nat. Commun.* **2017**, *8*, 15093.
46. Cuscó, R.; Alarcón-Lladó, E.; Ibanez, J.; Artús, L.; Jimenez, J.; Wang, B.; Callahan, M. J. Temperature Dependence of Raman Scattering in ZnO. *Phys. Rev. B* **2007**, *75*, 165202.
47. Lee, C.; Yan, H.; Brus, L. E.; Heinz, T. F.; Hone, J.; Ryu, S. Anomalous Lattice Vibrations of Single-and Few-Layer MoS_2. *ACS Nano* **2010**, *4*, 2695-2700.
48. Rice, C.; Young, R.; Zan, R.; Bangert, U.; Wolverson, D.; Georgiou, T.; Jalil, R.; Novoselov, K. Raman-Scattering Measurements and First-Principles Calculations of Strain-Induced Phonon Shifts in Monolayer MoS_2. *Phys. Rev. B* **2013**, *87*, 081307.
49. Wang, Y.; Cong, C.; Qiu, C.; Yu, T. Raman Spectroscopy Study of Lattice Vibration and Crystallographic Orientation of Monolayer MoS_2 under Uniaxial Strain. *Small* **2013**, *9*, 2857-2861.
50. He, K.; Poole, C.; Mak, K. F.; Shan, J. Experimental Demonstration of Continuous

Electronic Structure Tuning *via* Strain in Atomically Thin MoS_2. *Nano Lett.* **2013**, *13*, 2931-2936.

51. Mohiuddin, T.; Lombardo, A.; Nair, R.; Bonetti, A.; Savini, G.; Jalil, R.; Bonini, N.; Basko, D.; Galiotis, C.; Marzari, N. Uniaxial Strain in Graphene by Raman Spectroscopy: G Peak Splitting, Grüneisen Parameters, and Sample Orientation. *Phys. Rev. B* **2009**, *79*, 205433.
52. Bang, S.; Duong, N. T.; Lee, J.; Cho, Y. H.; Oh, H. M.; Kim, H.; Yun, S. J.; Park, C.; Kwon, M.-K.; Kim, J.-Y. Augmented Quantum Yield of a 2D Monolayer Photodetector by Surface Plasmon Coupling. *Nano Lett.* **2018**, *18*, 2316-2323.
53. Zhang, X.; Liao, Q.; Kang, Z.; Liu, B.; Ou, Y.; Du, J.; Xiao, J.; Gao, L.; Shan, H.; Luo, Y.; Fang, Z.; Wang, P.; Sun, Z.; Zhang, Z.; Zhang, Y. Self-Healing Originated van der Waals Homojunctions with Strong Interlayer Coupling for High-Performance Photodiodes. *ACS Nano* **2019**, *13*, 3280-3291.
54. Mak, K. F.; He, K.; Lee, C.; Lee, G. H.; Hone, J.; Heinz, T. F.; Shan, J. Tightly Bound Trions in Monolayer MoS_2. *Nat. Mater.* **2013**, *12*, 207-211.
55. Ly, T. H.; Yun, S. J.; Thi, Q. H.; Zhao, J. Edge Delamination of Monolayer Transition Metal Dichalcogenides. *ACS Nano* **2017**, *11*, 7534-7541.
56. Conley, H. J.; Wang, B.; Ziegler, J. I.; Haglund Jr, R. F.; Pantelides, S. T.; Bolotin, K. I. Bandgap Engineering of Strained Monolayer and Bilayer MoS_2. *Nano Lett.* **2013**, *13*, 3626-3630.
57. Du, J. L.; Liao, Q. L.; Hong, M. Y.; Liu, B. S.; Zhang, X. K.; Yu, H. H.; Xiao, J. K.; Gao, L.; Gao, F. F.; Kang, Z.; Zhang, Z.; Zhang, Y. Piezotronic Effect on Interfacial Charge Modulation in Mixed-Dimensional van der Waals Heterostructure for Ultrasensitive Flexible Photodetectors. *Nano Energy* **2019**, *58*, 85-93.
58. Kümmell, T.; Hutten, U.; Heyer, F.; Derr, K.; Neubieser, R. M.; Quitsch, W.; Bacher, G. Carrier Transfer across a 2D-3D Semiconductor Heterointerface: The Role of Momentum Mismatch. *Phys. Rev. B* **2017**, *95*, 081304.
59. Look, D. C. Recent Advances in ZnO Materials and Devices. *Mater. Sci. Eng., B*

2001, *80*, 383-387.

60. Zhu, J.; Wang, Z.; Yu, H.; Li, N.; Zhang, J.; Meng, J.; Liao, M.; Zhao, J.; Lu, X.; Du, L. Argon Plasma Induced Phase Transition in Monolayer MoS_2. *J. Am. Chem. Soc.* **2017**, *139*, 10216-10219.
61. Lanzillo, N. A.; Simbeck, A. J.; Nayak, S. K. Strain Engineering the Work Function in Monolayer Metal Dichalcogenides. *J. Phys.: Condens. Matter* **2015**, *27*, 175501.
62. Kang, Z.; Si, H.; Shi, M.; Xu, C.; Fan, W.; Ma, S.; Kausar, A.; Liao, Q.; Zhang, Z.; Zhang, Y. Kelvin Probe Force Microscopy for Perovskite Solar Cells. *Sci. China Mater.* **2019**, *62*, 776-789.
63. Zhang, Y.; Yan, X.; Yang, Y.; Huang, Y.; Liao, Q.; Qi, J. Scanning Probe Study on the Piezotronic Effect in ZnO Nanomaterials and Nanodevices. *Adv. Mater* **2012**, *24*, 4647-4655.
64. Henck, H.; Aziza, Z. B.; Zill, O.; Pierucci, D.; Naylor, C. H.; Silly, M. G.; Gogneau, N.; Oehler, F.; Collin, S.; Brault, J. Interface Dipole and Band Bending in the Hybrid *p-n* Heterojunction MoS_2/GaN(0001). *Phys. Rev. B* **2017**, *96*, 115312.

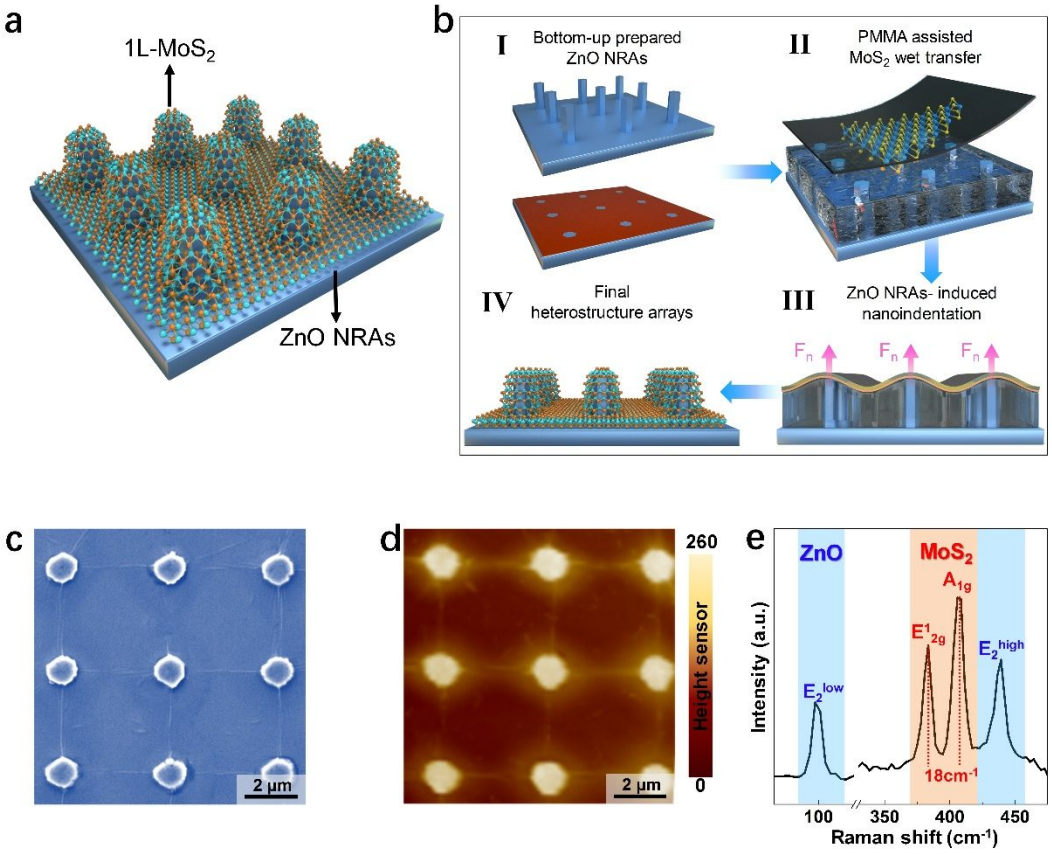

Figure 1. Fabrication and characterization of periodically strain-engineered 1L-MoS_2/ZnO heterostructure arrays. (a) The schematic of the 1L-MoS_2/ZnO heterostructure arrays. (b) The construction process of the 1L-MoS_2/ZnO heterostructure arrays. (c) The false-colour SEM image of ZnO NRAs covered by as-transferred 1L-MoS_2. (d) The AFM topography of the 1L-MoS_2/ZnO nanorod heterostructure arrays. (e) Raman scattering of the 1L-MoS_2/ ZnO heterostructure arrays under 532 nm laser excitation.

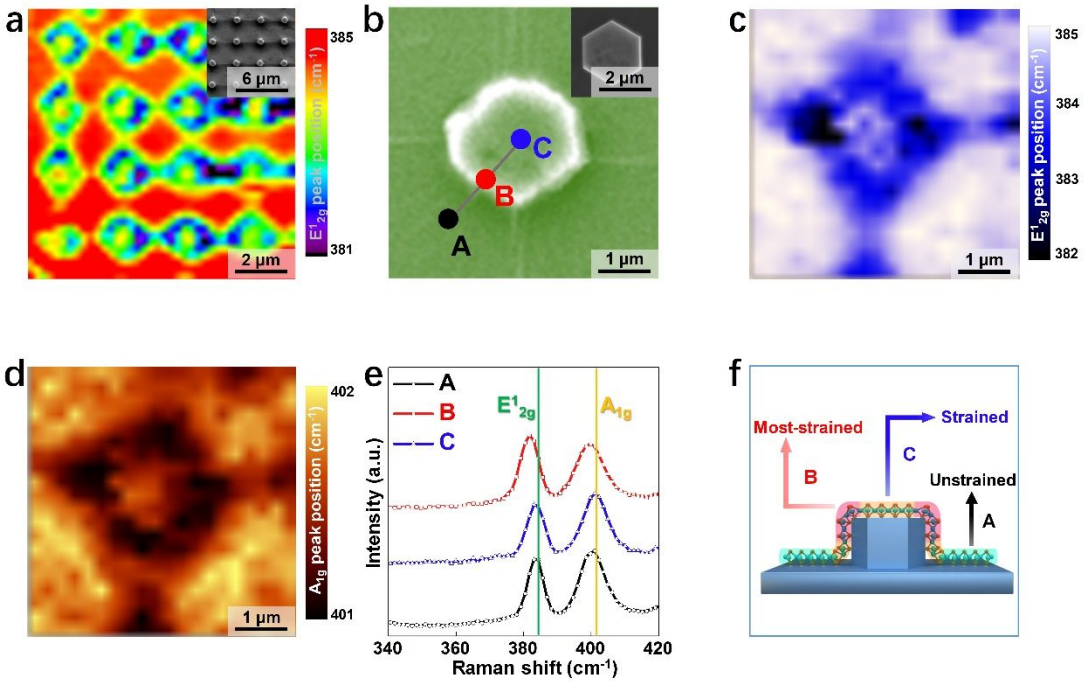

Figure 2. Confocal Raman measurements of the MoS_2/ZnO heterostructure arrays for strain distribution analysis. (**a**) Raman mapping of the E^1_{2g} peak position shift of 1L-MoS_2 on the ZnO NRAs (λ_{ex} = 532 nm). Inset: True SEM image of 1L-MoS_2 on the 4 × 4 ZnO NRAs. (**b**) The false-colour SEM image of 1L-MoS_2 on the single ZnO nanorod. Inset: The SEM image of the single as-grown ZnO nanorod crystal. Scanning Raman spectroscopic maps plotting (**c**) E^1_{2g} peak frequency and (**d**) A_{1g} peak frequency shift of MoS_2 on the single ZnO nanorod. (**e**) Raman spectra of 1L-MoS_2 at region (A, B, C) under different strain. Symbols are measurement data; curves are fitting data. (**f**) The schematic of strain distribution of 1L-MoS_2 at different regions of the patterned ZnO substrate.

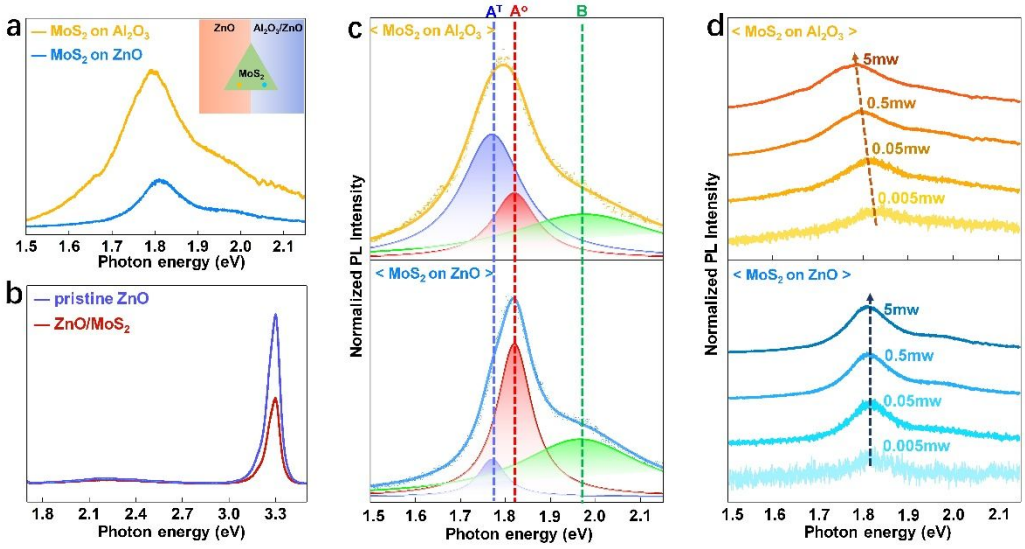

Figure 3. Determination of the interfacial charge transfer between 1L-MoS_2 and ZnO. (**a**) The PL spectra of 1L-MoS_2 on the ZnO and on the Al_2O_3/ZnO under 532 nm excitation. Inset: The schematic of the 1L-MoS_2 on the different substrates (ZnO and Al_2O_3/ZnO). (**b**) The PL spectra of ZnO with MoS_2 and pristine ZnO under 325 nm excitation. (**c**) Each fitted PL spectrum of 1L-MoS_2 on the Al_2O_3/ZnO (top) and on the ZnO (bottom) by Lorentzian functions for the B exciton (~1.97 eV), neutral exciton (A^o, ~1.83 eV) and trion (A^T, ~1.78 eV) peaks. Symbols are measurement data; curves are fitting data. (**d**) Power-dependent (0.005-5 mW) PL spectra of the 1L-MoS_2 on the Al_2O_3/ZnO (top) and on the ZnO (bottom).

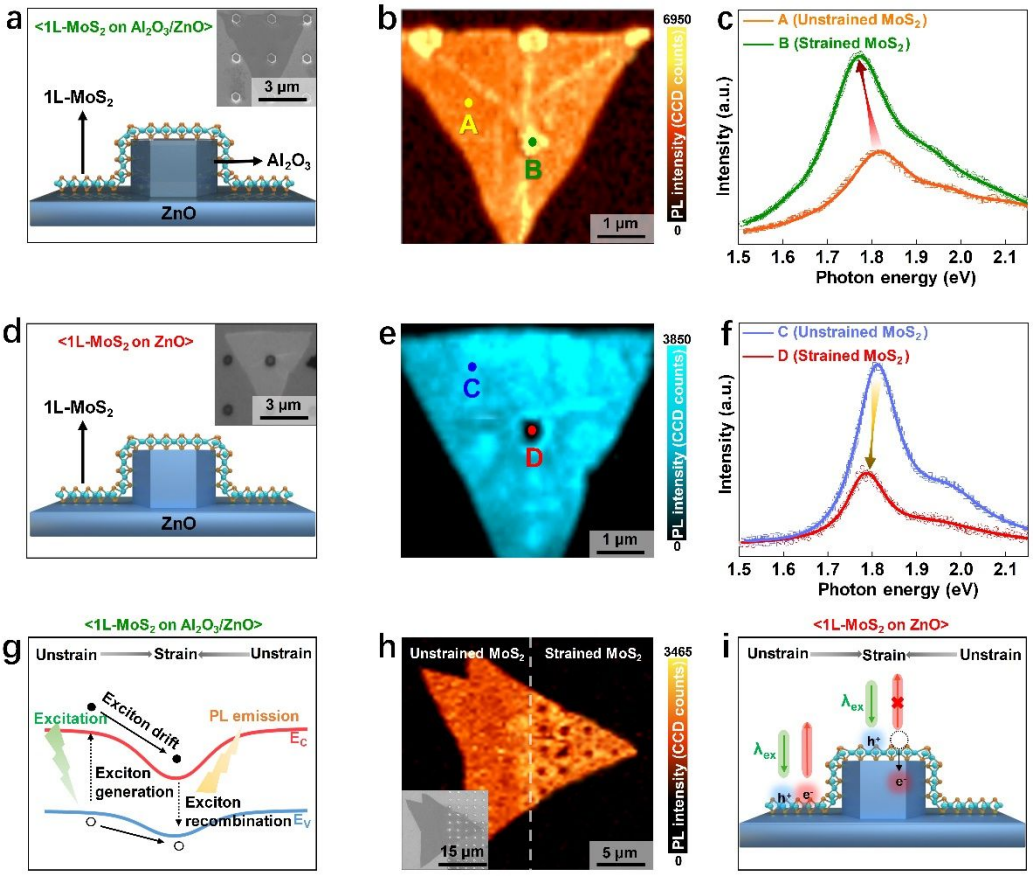

Figure 4. Confocal PL measurements of strain-engineered heterointerfaces. (**a**) The schematic of 1L-MoS_2 on the 10 nm Al_2O_3-coated ZnO NRAs. Inset: The true SEM image of 1L-MoS_2 on the ZnO NRAs. (**b**) Scanning PL maps with integrated peak intensity (1.75-1.85 eV) of the 1L-MoS_2 on the 10 nm Al_2O_3/ZnO nanorods substrate. (**c**) PL spectra of 1L-MoS_2 in region A (unstrained 1L-MoS_2) and B (strained 1L-MoS_2). Symbols are measurement data; curves are fitting data. (**d**) The schematic of 1L-MoS_2 on the single ZnO nanorod. Inset: Optical image of 1L-MoS_2 on the ZnO NRAs. (**e**) Scanning PL maps with integrated peak intensity (1.75-1.85 eV) of the MoS_2 on the ZnO nanorods substrate. (**f**) PL spectra of MoS_2 in region C (unstrained 1L-MoS_2) and D (strained 1L-MoS_2). (**g**) The schematic diagram of the strain-induced exciton funneling process of 1L-MoS_2 on the Al_2O_3 coated ZnO NRAs. (**h**) Scanning PL maps with integrated peak intensity (1.75-1.85 eV) of the 1L-MoS_2 on the boundary between unstrained (on the ZnO substrate) and strained 1L-MoS_2 (on the ZnO NRAs). Inset: The SEM image of 1L-MoS_2 on the boundary between the ZnO substrate and the ZnO NRAs.

(**i**) The proposed mechanism of decreased PL intensity of strained 1L-MoS_2 on ZnO: more efficient charge transfers at the strain-engineered heterointerfaces.

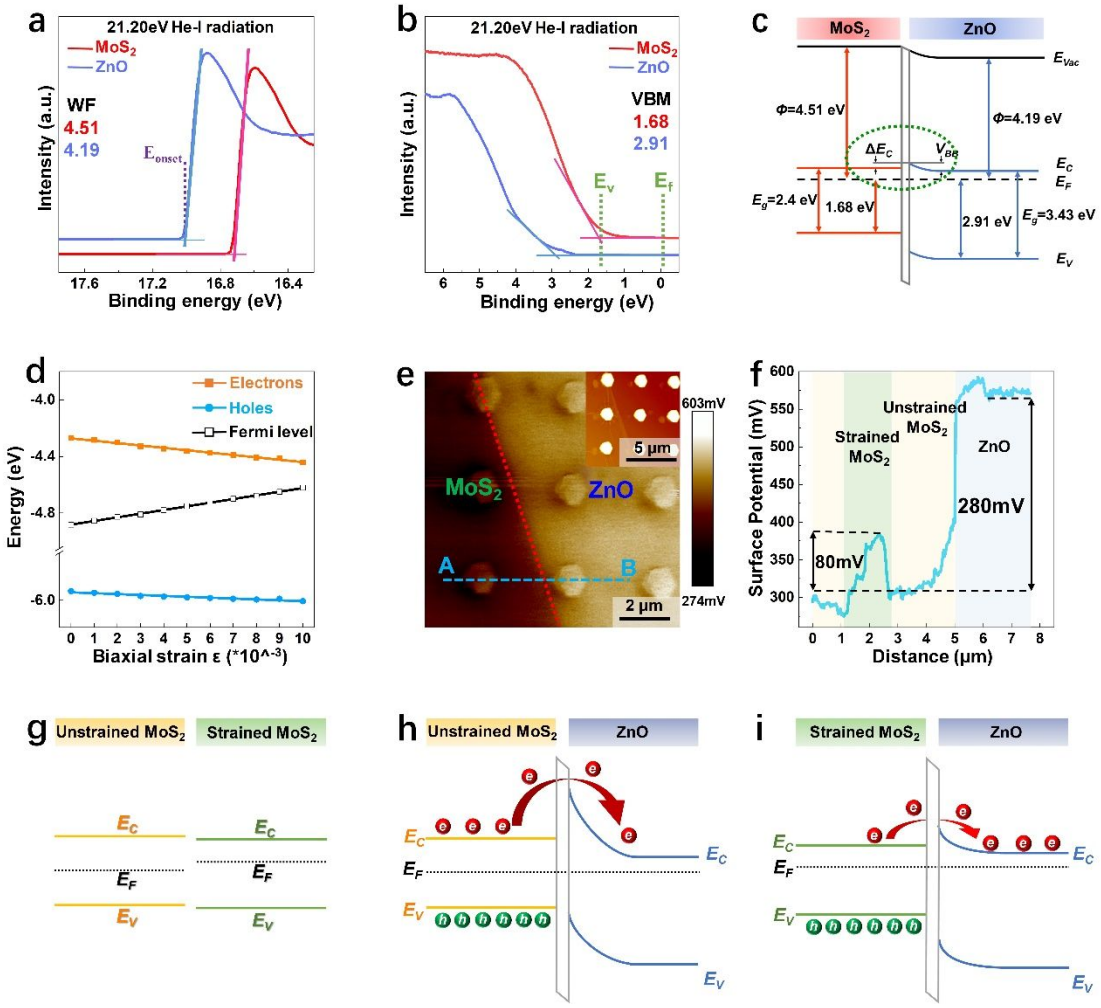

Figure 5. The mechanism of strain-enhanced interfacial charge transfer. (**a**) The work function and the energy difference (**b**) between the Fermi level (E_F) and valence band maximum (E_{VBM}) of MoS_2 and ZnO illustrated by UPS. (**c**) Band diagram of 1L-MoS_2/ZnO heterojunction obtained by UPS measurements. (**d**) Biaxial strain-dependent energies for electrons, holes and Fermi level at the K point calculated using DFT. (**e**) KPFM image of the boundary between pristine ZnO NRAs and 1L-MoS_2/ZnO heterostructure arrays. Inset: AFM topography of the measured sample. (**f**) Surface potential profile across the MoS_2/ZnO boundary in panel **e**. (**g**) Comparison of band structures between pristine MoS_2 and strained MoS_2 based on theory calculations. (**h**) The schematic illustration of the interfacial charge transfer rate based on the band diagram of pristine 1L-MoS_2/ZnO. (**i**) The schematic illustration of the enhanced charge

transfer efficiency from strained 1L-MoS_2 to ZnO, which is originated from the reduction of the interfacial barrier height under strain modulation.

For Table of Contents Only